Phys Chem Minerals (2006) 33: 394–402
DOI 10.1007/s00269-006-0088-8

ORIGINAL PAPER

M. Texier · P. Cordier

TEM characterization of dislocations and slip systems in stishovite deformed at 14 GPa, 1,300°C in the multianvil apparatus

Received: 25 November 2005 / Accepted: 3 April 2006 / Published online: 7 July 2006

Abstract Transmission electron microscopy (TEM) has been used to investigate deformation microstructures of synthetic stishovite specimens deformed at 14 GPa, 1,300°C. Geometrical characteristics of numerous dislocations have been characterized by dislocation contrast and stereographic analyses in order to identify the easy slip systems of stishovite. TEM data allowed us to characterize the following slip systems: ⟨100⟩{001}, ⟨100⟩{010}, ⟨100⟩{021}, [001]{100}, [001]{110}, [001]{210} and ⟨110⟩{1$\bar{1}$0}. Observation of sub-grain boundaries and scalloped edge dislocations suggest that climb has been activated in the specimens.

Keywords Stishovite · Dislocation · Plasticity · Confining pressure · Twinning

Introduction

Plastic deformation of deep mantle phases is critical to our understanding of mantle convection which is an important component of the global dynamics of the Earth. In the mantle, stishovite is the stable phase of SiO_2 at pressure higher than 10 GPa, which corresponds to depths ranging from 300 km to 1,200–1,500 km. This mineral was first synthesized in the laboratory (Stishov and Popova 1961) and later observed in shocked specimens from terrestrial impact structures (Shoemaker and Chao 1961; Chao et al. 1962; Chao and Littler 1963). It is also present in some shocked Martian meteorites (Langenhorst and Poirier 2000; El Goresy et al. 2004; Beck et al. 2004; Aoudjehane et al. 2005).

Stishovite is not expected to be a major constituent of the bulk mantle, but it may be present in significant amounts in subducted MORB's (Ringwood 1991). Stishovite is also a mineral of prime interest as a prototype phase of deep mantle silicates as it exhibits silicon in octahedral coordination.

Stishovite exhibits a rutile-type structure with space group $P4_2/mnm$ (Sinclair and Ringwood 1978). Stishovite has a primitive tetragonal Bravais lattice with lattice parameters $a = b = 0.418$ nm and $c = 0.26678$ nm (Ross et al. 1990). The SiO_6 octahedra form edge-shared chains along the c-axe that are each connected to four other parallel chains.

Several techniques have become available to deform minerals in pressure–temperature conditions which are relevant to the earth's deep mantle (see a recent review in Cordier et al. 2005). Among those, the Kawai-type, multianvil apparatus can reach confining pressures up to 25 GPa hence covering the conditions of the transition zone and of the uppermost lower mantle. TEM examination of stishovite synthesized in such apparatus has allowed us to identify the stable dislocations of the stishovite structure (Cordier and Sharp 1998). Specific deformation experiments have then been conducted on stishovite for which only preliminary TEM characterizations have been reported so far (Cordier et al. 2004).

The aim of the present study is to present an extensive characterization of the dislocations and slip systems activated in stishovite deformed at 14 GPa, 1,300°C.

Experimental procedure

Stishovite specimens were synthesized from wet (2,850 H/10^6 Si, see Mosenfelder 2000) silica glass in a Kawai multianvil apparatus (run S1926) at the Baye-

M. Texier · P. Cordier (✉)
Laboratoire de Structure et Propriétés de l'Etat Solide,
UMR CNRS 8008 - Bat C6, Université des Sciences et
Technologies de Lille, 59655 Villeneuve d'Ascq Cedex, France
E-mail: Patrick.Cordier@univ-lille1.fr
Tel.: +33-320-434341
Fax: +33-320-436591

P. Cordier
Bayerisches Geoinstitut, Universität Bayreuth,
Bayreuth, Germany

Present address: M. Texier
Laboratoire TECSEN, UMR 6122,
Université Aix-Marseille III,
13 397 Marseille Cedex 20, France

risches Geoinstitut. The initial glass cores were placed in rhenium capsules and annealed for over 10 h at 14 GPa and 1,300°C in a nominally hydrostatic high-pressure assembly. The pressure medium was a 14-mm octahedron of Cr-doped MgO that was compressed between eight cubic WC anvils with 8 mm truncation edge-lengths. High temperature was achieved by using a $LaCrO_3$ furnace surrounded by an insulating sleeve of ZrO_2. Temperature was measured using a $W_{97}Re_3$/$W_{75}Re_{25}$ thermocouple contained axially in the top alumina piston. The recovered stishovite sample was then placed into a compression assembly specifically designed to apply non-hydrostatic stresses onto the specimen. This deformation assembly differs from the standard 14/8 assembly described above as the specimen is placed between two hard alumina pistons (see Cordier and Rubie 2001). Specimens were plastically deformed at 1,300°C under a confining pressure of 14 GPa (run H 913). In these experiments, stress and strain cannot be directly (in situ) controlled nor measured, and most of the information are withdrawn from microstructural characterization of recovered samples. Previous experiments have shown that high stresses are generated during cold compression that can induce some cold deformation. These stresses are relaxed at high-temperature by plastic deformation of the specimen (Thurel and Cordier 2003; Couvy et al. 2004). Due to the small dimensions of the pressure cell, the experiments can be quenched very rapidly, thus offering very good preservation of the deformation microstructures compared to most conventional experiments.

Thin sections containing the deformation axis were prepared from slices, cut from the middle of the run product, by mechanical grinding. Final optical-quality polishing was achieved with diamond paste abrasive. The obtained 30-μm foils were then glued with epoxy on center-bored copper grids. Thinning of the samples was achieved using a Gatan Mod. 600 ionic milling device at 5 kV, under a low beam angle of 15° in order to obtain electron transparency of parts of the foils. TEM observations were performed in Lille in two-beam conditions using a JEOL 200 CX electron microscope and a FEI TECNAI G2 electron microscope operating at 200 kV.

The dislocation Burgers vectors **b** were determined using the relation $\mathbf{g} \cdot \mathbf{b} = 0$, where **g** is the diffraction vector, verified when the dislocations are out of contrast.

The line directions **u** of dislocation were determined from various TEM micrographs corresponding to projected images of the microstructure along several orientations. The determination of the incident electron beam direction $\mathbf{e_i}$ provides, for each micrograph, the indexation of the plane $\mathbf{P_i}$ containing the electron beam and the dislocation line directions. The dislocation line direction is then identified as the intersection of at least two planes $\mathbf{P_i}$ obtained with different specimen orientations.

The glide plane is then defined as the plane containing both the line direction **u** of the dislocation and its Burgers vector **b**.

It must be emphasized that stishovite specimens are very sensitive to electron irradiation. Consequently, TEM observations have been achieved quickly under low-dose conditions in order to reduce beam damage.

Results

Optical scale

Synthesis of stishovite from the wet silica glass resulted in a relatively coarse-grained material (average grain size, around 5–10 μm). Some grains could actually grow very much as they reached the maximum dimensions allowed in the pressure capsule (≈ 1 mm). Figure 1 shows such an example of a crystal extracted from a synthesis experiment (run S1925) performed in the same experimental conditions as run S1926. It is shown that stishovite grains tend to grow faster along the c direction. Only grains which nucleated early could grow freely whereas further crystals had to fit in the available space. It is important to point out that hydrogen-free samples (as checked by infrared spectroscopy in the 4,500–2,500 cm^{-1} spectral range) are produced although the starting material was containing a large amount of H-bearing species. This is probably due to the long annealing time which allowed water to escape from the capsule.

The occurrence of plastic deformation can be inferred from optical examination as many grains exhibit clear undulose extinction contrast under crossed Nichols (see Fig. 2a). Some grains show twins lamellae which are likely being due to deformation as they have never been observed in unstrained samples (Fig. 2b). Most grains are un-twinned, however, especially those observed at the TEM scale. The following of this article will thus be focused on dislocation microstructures only.

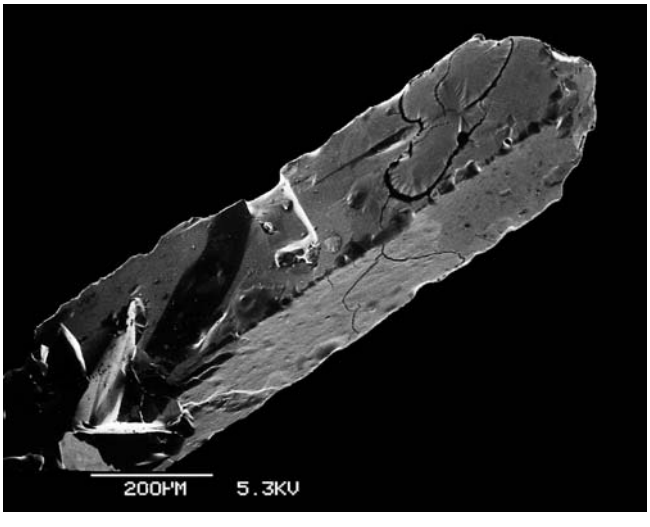

Fig. 1 Scanning electron micrograph of a stishovite single crystal synthesized at 14 GPa, 1,300°C (run S1925) and extracted from the capsule

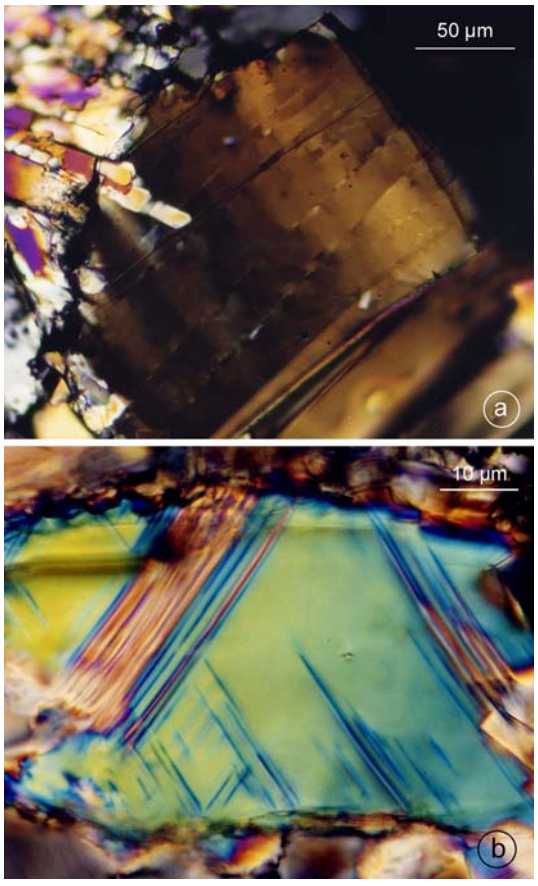

Fig. 2 Optical micrographs. **a** Undulose extinction suggesting plastic deformation by dislocation creep. **b** Twin lamellae are clearly visible in some grains

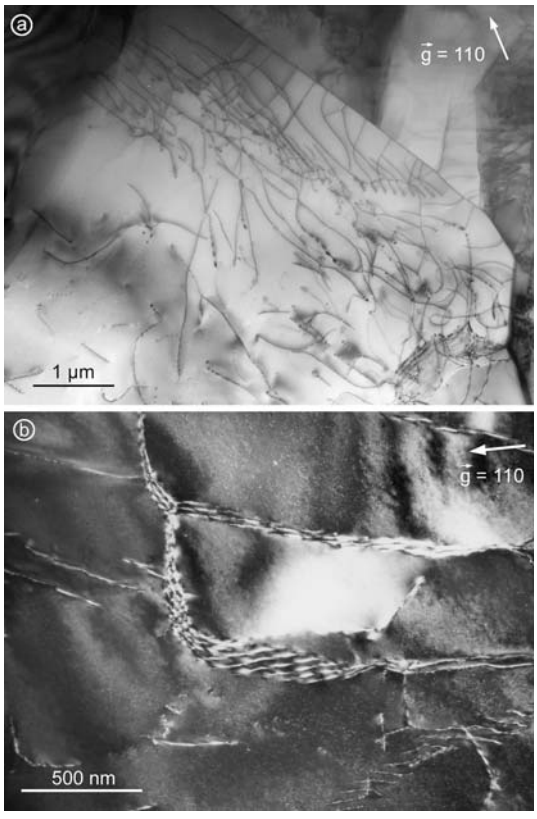

Fig. 3 Examples of deformation microstructures. **a** First stages of dislocation network formation. Bright-field TEM micrograph, **g** parallel to [110]*. **b** Numerous grains contain sub-grain boundaries. Some dislocations are curved in several sub-grain boundaries, i.e., lye in different glide planes. Dark-field TEM micrograph, **g** parallel to [110]*

TEM scale

Microstructural investigation was performed in the TEM in various areas of several thin foils. Sampling of the investigated areas permitted to discriminate the representative events produced by plastic deformation. Nevertheless, the important variation of defect densities observed from one grain to another indicates that plastic deformation was heterogeneously produced in the specimens during deformation.

The main microstructural features are listed below:

- In the most parts of the specimen, numerous dislocations are observed, forming in some cases poorly-organized dislocation networks (see Fig. 3a).
- Free dislocations, apparently lying in common slip planes are also found.
- Many grains exhibit long and well equilibrated sub-grain boundaries. These sub-grain boundaries often contain dislocations with line segments belonging to several planes (see Fig. 3b).

Dislocation densities have been estimated using the method of Ham (1961) based on the superimposition of a periodic square network onto the TEM images. Counting the number of intersections between the dislocation lines and the network gives the local dislocation density ρ using the relation:

$$\rho = \frac{2n}{Lt}, \tag{1}$$

where n is the number of intersections, L is the total length of the network lines and t is the average thickness of the foil in the observed area.

Dislocation densities vary from grain to grain. Total dislocation densities, regardless on the nature of dislocations, have been measured in different investigated area and fluctuate between 3.3×10^{11} and 2.1×10^{13} m^{-2}. Only few grains exhibit dislocation densities that can be significantly lower than the precedent values.

Contrast analysis of the dislocations has been made in two-beam conditions using various diffraction vectors **g**. As seen below, the studied dislocations present different Burgers vectors defining three distinctive families. The proportion of each family depends on the investigated area.

[001] Dislocations

Extinctions of most observed dislocations were obtained with **g** parallel to ⟨100⟩, ⟨110⟩ and ⟨120⟩ directions

according to our indexation conditions, indicating that their Burgers vectors are parallel to the [001] axis (see Figs. 4, 5, 6).

The main dislocation characters (that is edge, screw or mixed) have been deduced from the identification of the line directions. Representative examples are reported in Table 1.

The character of [001] dislocations is rather complex. Dislocations with a dominant edge character are mainly found in the {100} planes and those observed in the {110} planes present a dominant screw character. No significant character is found for dislocations lying in the {210} planes where very variable situations are observed.

Determination of various dislocation line directions allowed us to distinguish the following slip systems: [001](100), [001](110), [001](1$\bar{1}$0), [001](210) and [001](2$\bar{1}$0).

⟨100⟩ Dislocations

Although less abundantly observed than [001] dislocations, [100] (or [010] which are formally equivalent) dislocations were also identified in various areas of the deformed specimens. Their occurrence is variable from grain to grain. Whereas only [001] dislocations were observed in the area showed in Fig. 5, dislocation densities of [100], [010] and [001] dislocations are found to be very similar in other grains. For instance, dislocations densities of the previously reported dislocation families are, respectively, 1.1×10^{11}, 1.3×10^{11} and 0.9×10^{11} m^{-2} in the grain shown in Fig. 6.

The character of ⟨100⟩ dislocations depends on the dislocation habit plane (see Table 1). ⟨100⟩ dislocations often present a pure edge character when lying in (001) or {010} planes. However, they are mixed in the {021} glide planes.

One can also observe some ⟨100⟩ dislocations exhibiting a scalloped shape (see Fig. 7). The line undulations strongly depend on the dislocation line orientation, thus on the dislocation character. The dislocation segments which present a sinuous shape are mostly of dominant or pure edge character, as observed for dislocations on Fig. 7 (see also Table 1 for the line orientations). On the contrary, screw parts of the dislocations are straight, as seen for the dislocation numbered 5.

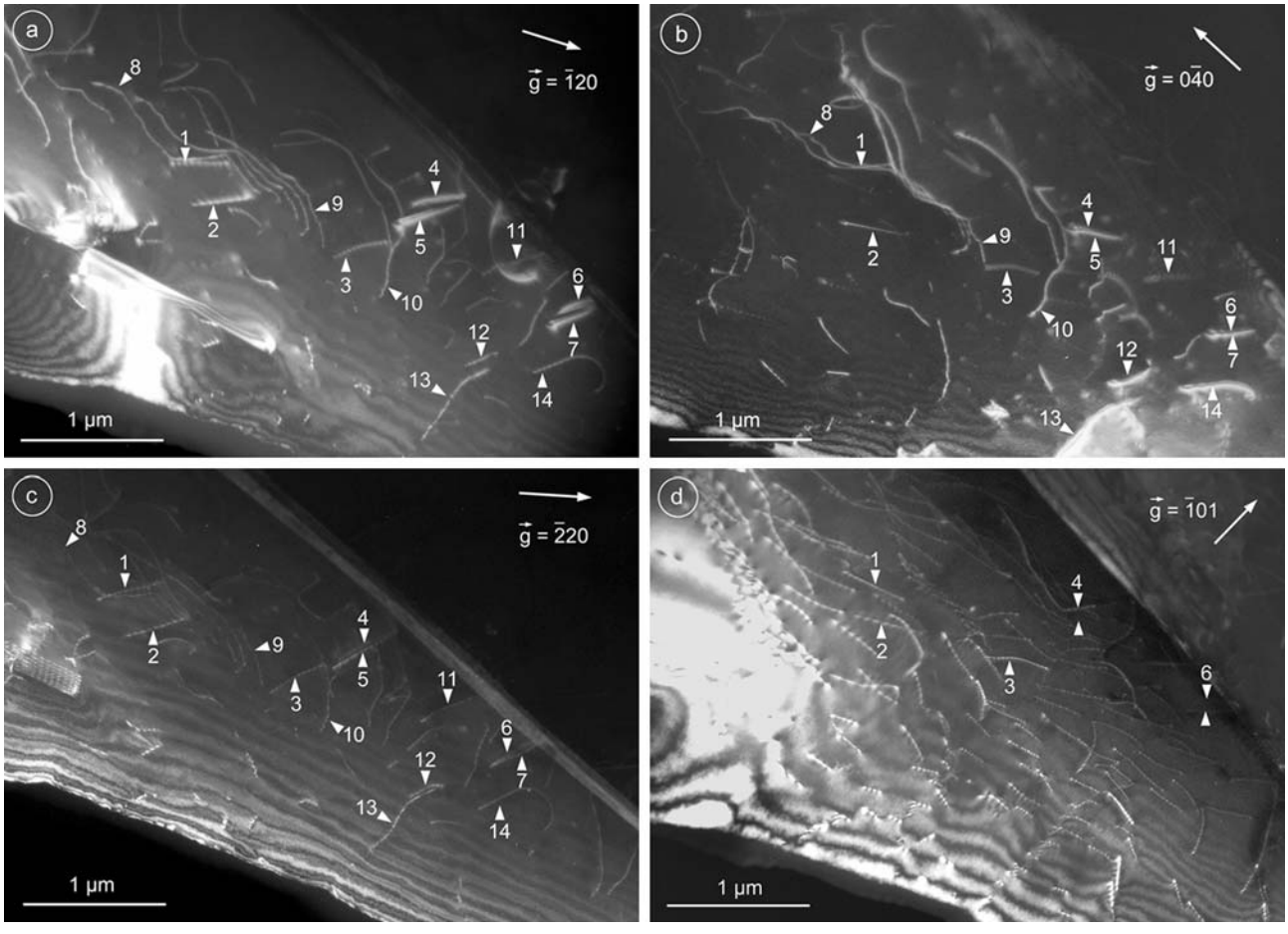

Fig. 4 Weak-beam dark-field TEM micrographs of an area containing both [100], [010] and [001] dislocations **a** $\mathbf{g} = [\bar{1}20]^*$, $\mathbf{s} = 5.35$ nm^{-1}. **b** $\mathbf{g} = [0\bar{4}0]^*$, $\mathbf{s} = 4.79$ nm^{-1}. **c** $\mathbf{g} = [\bar{2}20]^*$, $\mathbf{s} = 3.38$ nm^{-1}. **d** $\mathbf{g} = [\bar{1}01]^*$, $\mathbf{s} = 4.45$ nm^{-1}. Dislocations [110] (numbered *1–7* on the figures) are visible with the four diffraction vectors used. **a**, **b**, **c** Dislocations [001] are out of contrast. **d** Dislocations [010] (numbered *8–14* on the figures) are out of contrast

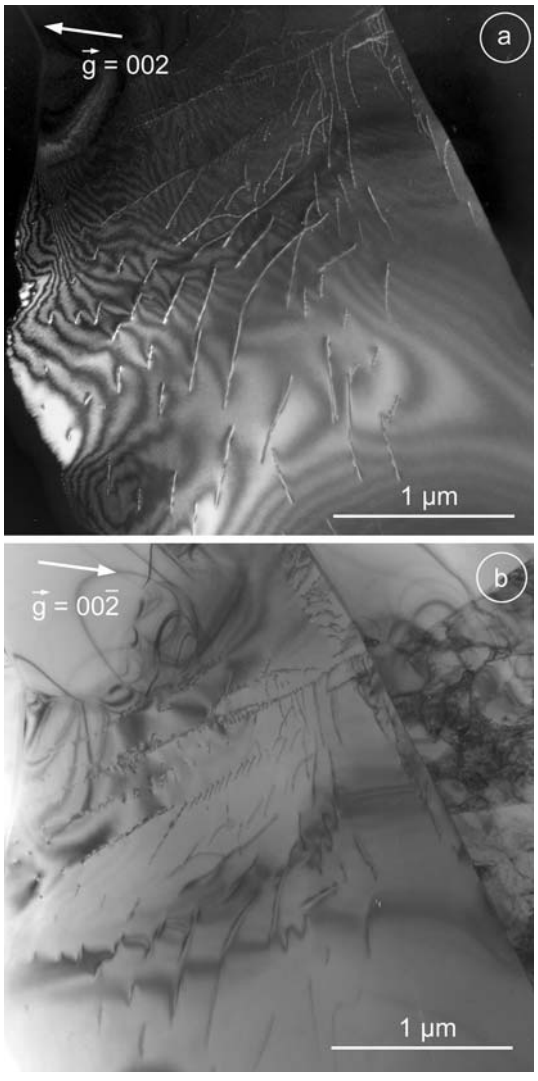

Fig. 5 [001] Dislocations. **a** Weak-beam dark-field TEM micrograph using the [002]* diffraction vector ($\mathbf{s} = 7.50\ \mathrm{nm}^{-1}$). **b** Bright-field TEM micrograph, $\mathbf{g} = [00\bar{2}]^*$. This area presents [001] dislocations lying in five different slip planes. Sub-grain boundaries visible on these micrographs also contain [001] dislocations

Determination of few line directions for each dislocation type leads to the following glide systems: [100](001), [100](021), [010]{100} and [010]{201}.

[110] Dislocations

The contrast of another dislocation family vanishes when using **g** parallel to $[\bar{1}01]$ and $[\bar{1}11]$ directions. This suggests that the Burgers vector of these dislocations is parallel to the [101] direction (see dislocations numbered 1 to 7 on Fig. 4). Line directions of few segments have been identified by stereographic analysis. Assuming that these dislocations moved by pure glide, the corresponding slip system is $[110](1\bar{1}0)$.

Discussion and conclusions

Slip systems

Most of the observed dislocations have [001] Burgers vectors. ⟨100⟩ dislocations are less abundantly observed, whereas ⟨110⟩ dislocations were found in only one grain, suggesting that they weakly participate to plastic deformation.

The dislocation activity appears to be strongly correlated with the dislocation elastic energy which scales with the square of the Burgers vector's modulus. Figure 8 shows that [001] dislocations (0.2667 nm) are approximately 2 times more favorable than ⟨100⟩ dislocations (0.418 nm) and at least 4 times more favorable than ⟨110⟩ dislocations (0.591 nm). These different Burgers vector lengths are responsible for the differences of contrast experimentally observed between [001] dislocations, which usually present a very fine contrast, and ⟨100⟩ or ⟨110⟩ dislocations which often show a stronger contrast.

Transmission electron microscopy characterization of dislocation line directions together with the Burgers vector directions leads to the identification of several glide systems which are summarized in Table 2 and illustrated in Fig. 9. From the observation abundance of the dislocations lying in each slip planes, the easiest slip systems appear to be [001]{100}, [001]{210}, followed by ⟨100⟩{010}, ⟨100⟩(001) and ⟨100⟩{021}.

Several factors can explain which slip systems are easily activated. Elastic anisotropy can be one reason. Stishovite is one of the most anisotropic high-pressure minerals (see Mainprice et al. 2000). Figure 8 shows the elastic energy for an edge dislocation in any plane containing the Burgers vector. The observed glide planes are arrowed. It is shown that for [001] and ⟨100⟩ slip, the elastic energy is very insensitive to the glide plane. Alternatively, the choice of the glide plane can be determined at the atomic level. Densities ρ_b of Si–O bond breaking associated with dislocation glide in the different slip planes may also constitute a key point that could favor certain slip planes for a given dislocation vector. The ρ_b values calculated for the various identified glide systems are reported in Table 2. Marked differences of ρ_b densities are found between planes suggesting a possible hierarchy among them. We don't have enough observations to further support or deny this hypothesis. The occurrence of $\langle 110\rangle\{1\bar{1}0\}$ glide, very unlikely from the elastic energy point of view, could result from the relatively low bond density in the {110} planes. It is likely, however, that ⟨110⟩ slip has been activated in the high stress regime during compression, or at the very beginning of the deformation experiment as observed by Thurel et al. (2003b) in the case of wadsleyite deformed under comparable conditions.

It is interesting to compare plastic anisotropy of stishovite with the one exhibited by other minerals with the

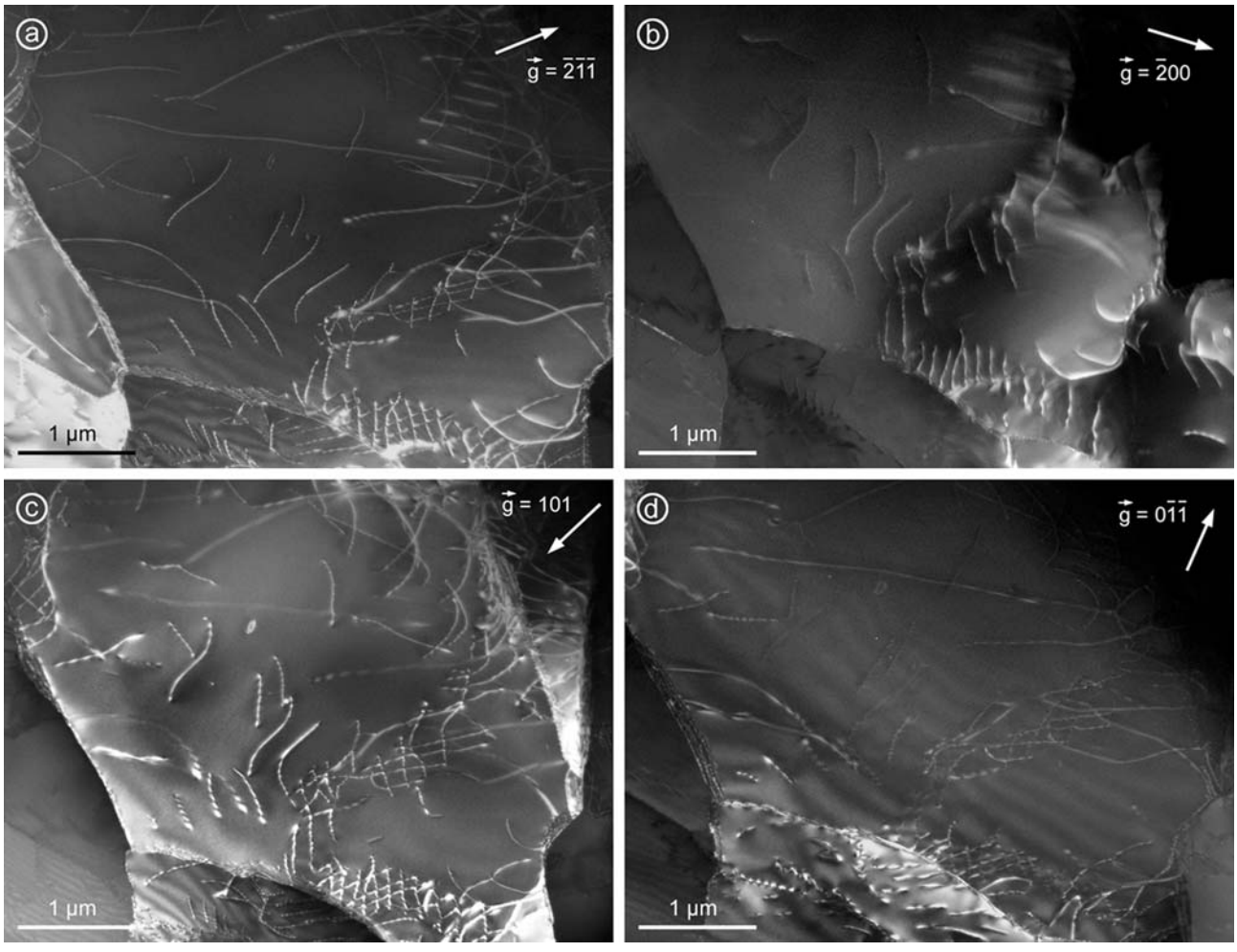

Fig. 6 TEM images of [100], [010] and [001] dislocations observed in the same grain. Ninety-five dislocations have been analyzed in this area. **a** Dark-field TEM micrograph, $\mathbf{g} = [\bar{2}\bar{1}\bar{1}]^*$. [100], [010] and [001] dislocations are visible. **b** Weak-beam dark-field TEM micrograph, $\mathbf{g} = [\bar{2}00]^*$, $\mathbf{s} = 4.79\ \mathrm{nm}^{-1}$. Only [100] dislocations are in contrast. **c** Weak-beam dark-field TEM micrograph, $\mathbf{g} = [101]^*$, $\mathbf{s} = 4.45\ \mathrm{nm}^{-1}$. [010] dislocations are out of contrast. **d** Weak-beam dark-field TEM micrograph, $\mathbf{g} = [0\bar{1}\bar{1}]^*$, $\mathbf{s} = 4.45\ \mathrm{nm}^{-1}$. [100] dislocations are out of contrast

rutile structure. The plastic properties of TiO_2 rutile have been studied in the 800–1,700 K temperature range using creep experiments which differ significantly from our experimental conditions. Less slip systems have been reported in TiO_2 rutile than in stishovite: ⟨101⟩{101} (the easiest) and [001]{110} (Ashbee and Smallman 1963; Blanchin et al. 1980). Paratellurite TeO_2 is tetragonal with $a = 0.48$ nm and $c = 0.76$ nm. It can be considered as a slightly distorted rutile structure in which two "rutile-like" unit cells are stacked along the [001] axis (Péter et al. 1986). Possible Burgers vectors in this structure are ⟨010⟩ and ⟨110⟩. Optical microscopy and X-ray topography suggest glide on {100}, (001), {101} and {110}. ⟨010⟩(001) are the easiest glide systems in paratellurite TeO_2. Although more experiments on these materials would be necessary to confirm this view, the rutile group does not appear to constitute an analog series for plastic deformation.

Deformation mechanisms

Figure 2b shows that mechanical twinning is one of the possible deformation mechanisms of stishovite. The present discussion focuses on dislocation activity only. Detailed characterizations of dislocation line directions have led to the identification of the glide planes and shown that dislocation glide was the dominant deformation mechanism in our sample. The observation of preferential line orientations is important as it brings information on dislocation mobilities. Some preferential edge characters are found for ⟨100⟩(001) and ⟨100⟩{010} as well as for [001]{100} dislocations whereas screw characters are more characteristic of [001]{110}. This would suggest a lower mobility for these dislocations. However, dislocation loops do not seem to have very anisotropic mobilities in stishovite. It is difficult with such microstructure to assess the importance of lattice

Table 1 Characteristics of the [001] and [010] dislocations shown in Fig. 6

Number	**b**	Line direction	Glide plane	Dislocation character/α = (**b**,**u**)
1	[100]	$\mathbf{u_2} = [1\bar{2}4]$	(021)	Almost edge/73°
2	[100]	$\mathbf{u_2} = [1\bar{2}4]$	(021)	Almost edge/73°
3	[100]	$\mathbf{u_3} = [0\bar{1}2]$	(021)	Edge/90°
		$\mathbf{u_4} = [010]$	(001)	Edge/90°
4	[100]	$\mathbf{u_4} = [010]$	(001)	Edge/90°
5	[010]	$\mathbf{u_1} = [0\bar{2}3]$	(100)	Mixed/44°
		$\mathbf{u_5} = [\bar{1}\bar{3}2]$	(201)	Almost screw/28°
6	[010]	$\mathbf{u_1} = [0\bar{2}3]$	(100)	Mixed/44°
[a]	[001]	$\mathbf{u} = [031]$	(100)	Almost edge/78°
		$\mathbf{u} = [114]$	$(1\bar{1}0)$	Almost screw/29°
		$\mathbf{u} = [\bar{1}13]$	(110)	Mixed/37°
		$\mathbf{u} = [\bar{1}23]$	$(2\bar{1}0)$	Mixed/49°
		$\mathbf{u} = [\bar{1}20]$	$(2\bar{1}0)$	Edge/90°
		$\mathbf{u} = [\bar{1}22]$	$(2\bar{1}0)$	Mixed/60°
		$\mathbf{u} = [\bar{1}23]$	$(2\bar{1}0)$	Mixed/49°

One can note that some dislocations (3 and 5) lye in more than one glide plane. Parameters of [001] dislocations observed in others areas are also reported

[a]Dislocations non-visible on Fig. 5

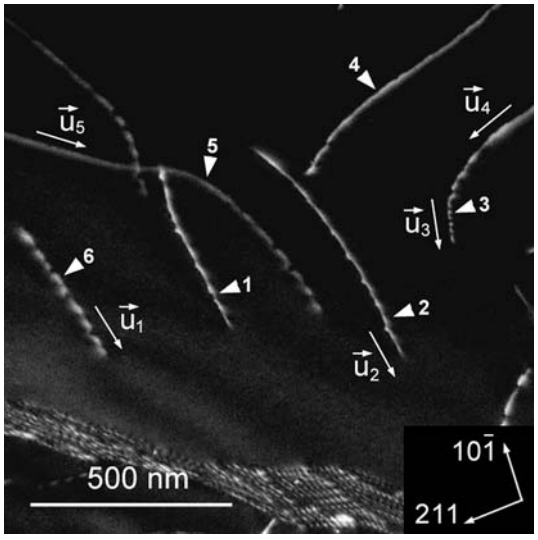

Fig. 7 Detail of Fig. 5a showing the undulations of [100] and [010] dislocation lines. Dislocations [100] are numbered *1–4* and dislocations [010] are numbered *5–6*. Dislocation character and corresponding slip plane according to the line directions labeled $\mathbf{u_1}$ to $\mathbf{u_5}$ are reported in Table 2

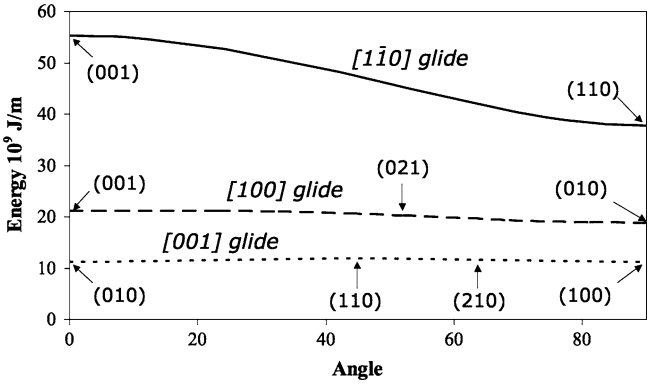

Fig. 8 Variation of the elastic energy for pure edge dislocations belonging to the [001]{hkl}, ⟨100⟩{h′ k′ l′} and ⟨110⟩{h″ k″ l″ } slip systems as a function of the angle between planes. Calculations performed with Disdi (Douin et al. 1986)

Table 2 Densities ρ_b of atomic bond breaking associated with dislocation glide in each identified glide system, given for different glide plane compactness (labeled type A or B, see Fig. 9)

Burgers vectors	Glide planes	ρ_b (nm^{-2})
⟨100⟩	{010}	Type A : 17.94
		Type B : 26.91
	(001)	22.89
	{021}	Type A : 21.18
		Type B : 24.71
[001]	{100}	Type A : 17.94
		Type B : 26.91
	{110}	Type A : 12.69
		Type B : 19.03
	{210}	Type A : 20.05
		Type B : 32.09
⟨110⟩	{1 $\bar{1}$0}	Type A : 12.69
		Type B : 19.03

friction which may affect every character with a comparable intensity.

It must be noted that the identified glide planes, which are intrinsically defined as the plane containing the dislocation line and Burgers vector directions, must be distinguished to the effective motion plane. Indeed, unambiguous identification of dislocation motion mechanisms that may locally occur is extremely difficult to obtain from *post mortem* TEM analyses. Even if deformation microstructures appear to mainly result from dislocation activity suggesting glide of dislocations, it is not possible to conclude that only dislocation glide is involved during deformation.

Indeed, some observations reported above point toward an other deformation mechanism. Figure 7 shows that in some cases screw parts are smooth whereas edge segments present a peculiar scalloped shape. The fact that these undulations affect edge segments only can be interpreted as an indication of the onset of climb by jog pair nucleation and propagation. The scalloped shape of the dislocations is then assumed to result from a slow propagation of the jog pairs compared to their nucleation rate. The presence of bent dislocations lying in different subgrain boundaries, as illustrated on Fig. 3b, further supports the hypothesis of dislocation climb. To understand this microstructure, it is important to remember that high-pressure deformation experiments in the multianvil apparatus are complex. Detailed microstructural observations from Thurel et al. (2003, 2003a) and Couvy et al. (2004) have shown that these experiments can be regarded as relaxation tests. High stresses are generated during cold compression that are relaxed during further annealing. The drawback is that

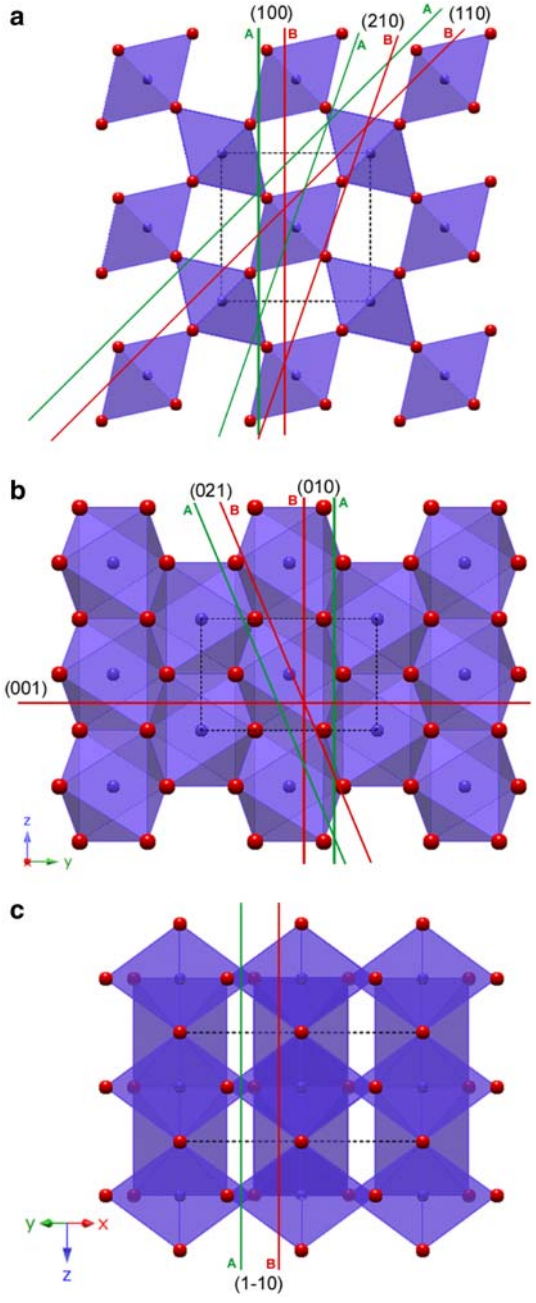

Fig. 9 Structure of stishovite seen along **a** [100], **b** [001] and **c** [110] directions, showing the silicon octahedral sites and the oxygen atomic positions. The different glide planes experimentally observed are seen edge on (**b** is parallel to the view directions)

the observed microstructures can be rather complicated (see the case of wadsleyite for instance: Thurel and Cordier 2003). The advantage is that the late deformation episodes correspond to very low strain-rate. It must be remembered that extrapolating laboratory data to Earth-relevant strain-rates is one of the most challenging issues of high-pressure experiments. Relaxation experiments offer an interesting possibility to approach such conditions. It is unlikely that completely new mechanisms (such as nucleation of new slip systems) can be enhanced in our experiments as low strain-rates necessarily correspond to small strains. However, dislocations lines must be the most sensitive probe to this low strain rate episode. For instance, slowly moving dislocation will have a greater tendency to lye in their Peierls valleys. This has motivated our attention on this parameter. The onset of dislocation climb is thus an important observation, although the contribution to the deformation of our sample is obviously negligible. The scalloped edge dislocations cannot glide any more (the jogs do not belong to the glide plane). At some point (most probably at the end of the experiment when the strain-rate became very low) the dislocations stopped gliding and began to climb. This might suggests that dislocation climb could be an important deformation mechanism of stishovite under mantle conditions.

Acknowledgements We thank J.L. Mosenfelder for his help in synthesising large-grained sthishovite. High-pressure experiments were performed at the Bayerisches Geoinstitut under the EU "Research Infrastructures: Transnational Access" Programme (Contract No. 505320 (RITA)-High Pressure). This work was supported by CNRS-INSU under the DyETI programme. Careful reviews from T.G. Sharp and A. El Goresy are gratefully acknowledged.

References

Aoudjehane HC, Jambon A, Reynard B, Blanc P (2005) Silica as a shock index in shergottites: a cathodoluminescence study. Meteor Planet Sci 40(7):967–979

Ashbee KHG, Smallman RE (1963) The plastic deformation of titanium dioxide single crystals. Proc R Soc A 274:195–205

Beck P, Gillet P, Gautron L, Daniel I, EI Goresy A (2004) A new natural high-pressure (Na,Ca)-hexaluminosilicate [$(Ca_x$-$Na_{1-x})Al_{3+x}Si_{3-x}O_{11}$] in shocked Martian meteorites. Earth Planet Sci Lett 219(1–2):1–12

Blanchin MG, Fontaine G, Kubin LP (1980) Dynamic strain aging in stoichiometric rutile single crystals. Philos Mag A 41:261–280

Chao ECT, Littler J (1963) Additional evidence for the impact origin of the Ries basin, Bavaria, Germany. Geol Soc Am Abstract, 127

Chao ECT, Fahey JJ, Littler J, Milton DJ (1962) Stishovite, SiO_2, a very high pressure new mineral from Meteor Crater, Arizona. J Geophys Res 67:419–421

Cordier P, Rubie DC (2001) Plastic deformation under extreme pressure using a multi-anvil apparatus. Mat Sci Eng A 309:38–43

Cordier P, Sharp TG (1998) Characterization of dislocations in stishovite by large angle convergent beam electron diffraction. Phys Chem Miner 25:548–555

Cordier P, Mainprice D, Mosenfelder JL (2004) Mechanical instability near the stishovite-$CaCl_2$ phase transition: implications for crystal preferred orientations and seismic properties. Eur J Mineral 16:387–399

Cordier P, Couvy H, Merkel S, Weidner D (2005) Plastic deformation of minerals at high pressure: experimental techniques. In: Miletich R (ed) Mineral behaviour at extreme conditions. EMU Notes in Mineralogy, vol 7, pp 1–42

Couvy H, Frost D, Heidelbach F, Nyilas K, Ungár T, Mackwell S, Cordier P (2004) Shear deformation experiments of forsterite at 11 GPa −1400°C in the multianvil apparatus. Eur J Mineral 16:877–889

Douin J, Veyssiére P, Beauchamp P (1986) Dislocation line stability in Ni_3Al. Philos Mag A 54:375–393

EI Goresy A, Dubrovinsky L, Sharp TG, Chen M (2004) Stishovite and post-stishovite polymorphs of silica in the Shergotty

meteorite: their nature, petrographic settings versus theoretical predictions and relevance to Earth's mantle. J Phys Chem Solids 65:1597–1608
Ham RK (1961) The determination of dislocation densities in thin films. Philos Mag 6:1183–1184
Langenhorst F, Poirier JP (2000) "Eclogitic" minerals in a shocked basaltic meteorite. Earth Planet Sci Lett 176:259–265
Mainprice D, Barruol G, Ben Ismal W (2000) Earth deep interior: mineral physics and tomography from the atomic scale to the global scale. In: Karato SI (ed) Geophysical Monograph American Geophysical Union, Washington, pp 237–264
Mosenfelder JL (2000) Pressure dependence of hydroxyl solubility in coesite. Phys Chem Miner 27:610–617
Péter A, Fries E, Jansky J, Castaing J (1986) Dislocations in paratellurite TeO_2: elastic energies and plastic deformation. Rev Phys Appl 21:289–298
Ringwood AE (1991) Phase transitions and their bearing on the constitution and dynamics of the mantle. Geochim Cosmochim Acta 55:2083–2110
Ross N, Shu J-F, Hazen RM (1990) High-pressure crystal chemistry of stishovite. Am Mineral 75:739–747
Shoemaker EM, Chao ECT (1961) New evidence for the impact origin of the Ries Basin, Bavaria, Germany. J Geophys Res 66:3371–3378
Sinclair W, Ringwood AE (1978) Single crystal analysis of the structure of stishovite. Nature 272:714–715
Stishov SM, Popova SV (1961) New dense polymorphic modification of silica. Geochemistry 10:923–926
Thurel E, Cordier P (2003) Plastic deformation of wadsleyite: I High-pressure deformation in compression. Phys Chem Miner 30:256–266
Thurel E, Cordier P, Frost D, Karato S (2003a) Plastic deformation of wadsleyite: II High-pressure deformation in shear. Phys Chem Miner 30:267–270
Thurel E, Douin J, Cordier P (2003b) Plastic deformation of wadsleyite: III. Interpretation of dislocations and slip systems. Phys Chem Miner 30:271–279